INTL JOURNAL OF ELECTRONICS AND TELECOMMUNICATIONS, 2026, VOL. 72, NO. 3, PP. 1-9
Manuscript received February 09, 2026; revised June, 2026. doi: 10.24425/ijet.2026.157947

Design of a compact four-port mmWave MIMO antenna with resonator-based band rejection

Janardhana Reddy Pandillapalli, and Kameswari Gummadi

***Abstract*—This paper introduces a compact ultra-wideband MIMO antenna featuring an integrated notch-band response. Wideband operation is achieved through the combined use of meandered feed lines, a modified Y-shaped radiating element, and a defected ground structure. The antenna occupies a compact volume of 12 x 8 x 1.6 mm³ and operates over the 30–42.5 GHz frequency range, while notch band from 35 to 38.5 GHz is effectively suppressed using a split-ring resonator positioned parallel to the feed line. Implemented on an RT/Duroid 5880 substrate, the antenna delivers a peak realized gain of 6.51 dB and maintains radiation efficiency above 88%. High inter-element isolation exceeding 22 dB is obtained through a dedicated decoupling structure. Moreover, the proposed MIMO system demonstrates strong diversity performance, with envelope correlation coefficient below 0.02, diversity gain greater than 9.97 dB. These characteristics confirm the suitability of the proposed antenna for compact 5G, satellite, and millimeter-wave communication platforms.**

***Keywords*—UWB; MIMO; SRR; Meandered feed line; mmWave**

I. Introduction

THE rapid advancement of wireless communication toward fifth-generation (5G) and beyond has increased the demand for high data rates, low latency, and enhanced connectivity. Millimeter-wave (mmWave) communication, operating from 30 to 300 GHz, provides substantially wider bandwidth and enables multi-gigabit data transmission, making it a key technology for future broadband systems. Owing to spectrum congestion in sub-6 GHz bands, mmWave frequencies have become essential for 5G deployment. In India, spectrum allocations at 3.3–3.67 GHz and 26.5–29.5 GHz further motivate the development of compact, low-profile, and high-efficiency antennas for next-generation wireless applications [1].

Numerous antenna design techniques have been reported to enhance impedance matching, bandwidth, and gain at millimeter-wave (mmWave) frequencies. Methods such as substrate integrated waveguide (SIW) cavities, stacked parasitic elements, and optimized microstrip-to-coplanar waveguide (CPW) transitions have demonstrated improved impedance matching and reduced surface-wave effects [2]–[4]. In addition, modified radiator geometries incorporating slots, notches, and parasitic features have been shown to excite multiple resonant modes, enabling wideband or multiband operation [5]–[7].

Multiple-input multiple-output (MIMO) technology plays a critical role in mmWave 5G systems by enhancing link reliability through spatial diversity and beamforming [8]. To achieve adequate isolation in compact MIMO configurations, several techniques—including neutralization lines, defected ground structures, and resonant decoupling elements—have been widely employed [9]–[12]. Bandwidth and radiation efficiency improvements have also been realized using partial ground planes, open-ended stubs, and slot-based structures, while optimization algorithms have been applied to fine-tune antenna parameters for enhanced performance [13]–[17]. Furthermore, various compact radiator geometries have demonstrated stable wideband performance around the 28 GHz and 38 GHz bands [18]–[22].

Despite the advantages of wideband operation, performance degradation may arise due to interference from overlapping frequency bands. Consequently, band-rejection mechanisms have been integrated using resonant structures such as split-ring resonators and frequency-selective elements to achieve sharp notch characteristics while preserving stable radiation behavior [23]–[25]. Alternative techniques employing embedded resonant slots and stubs have also been reported to suppress unwanted bands [26]–[28].

Recent studies emphasize the importance of millimeter-wave (mmWave) antennas for high-data-rate 5G and emerging 6G systems. However, mmWave antenna design is challenged by compact form factors, tight fabrication tolerances, and limited space for implementing conventional notch-generation techniques. In addition, wideband MIMO configurations, while essential for improving gain and diversity, often suffer from strong mutual coupling and in-band interference, making effective notch control increasingly critical. Conventional methods such as slots or parasitic resonators become less feasible at mmWave frequencies due to size constraints and structural complexity.

To address these challenges, a compact meandered line-fed patch antenna integrated with an externally coupled split-ring resonator (SRR) is proposed. The antenna employs a modified Y-shaped radiator and SRR-induced LC resonance to achieve controlled notch-band suppression without degrading the

First Author is with Department of ECE, RGUKT R.K. Valley Campus and Research Scholar, Department of ECE, JNT University Anantapur, Andhra Pradesh, India (e-mai:janardhanreddy1991@gmail.com).

Second Author is with NBKR Institute of Science & Technology, India (e-mail:kameswarigummadi@gmail.com)

primary radiation performance. The SRR provides strong inductive–capacitive coupling for precise rejection within the 35–38.5 GHz range, while the meandered feed enables wideband impedance matching within a compact footprint. This integrated approach achieves wide operational bandwidth with effective interference suppression, making it suitable for mmWave communication systems.

The rest of this paper is organized as follows. Section II presents the detailed design methodology of the single radiating element. Section III discusses the development of the proposed MIMO configuration along with the influence of isolation structure on mutual coupling performance. Section IV provides the simulated and measured results followed by a comprehensive discussion. Finally, Section V concludes the paper with key findings and potential directions for future work.

II. BASIC ANTENNA

A. Antenna Design

The designed antenna is realized using an RT/Duroid-5880 (εr = 2.2, loss tangent=0.0009) with dimensions of 6 x 4 mm^2 and a thickness of 1.6 mm is shown in Fig.1, associated dimensions are listed in Table I. It is comprised of modified Y-shaped radiating patch integrated with horizontal branch to the left arm and central branch connected with right arm of Y shaped Radiating patch, integrated with a meandered feed line and a defected ground plane.

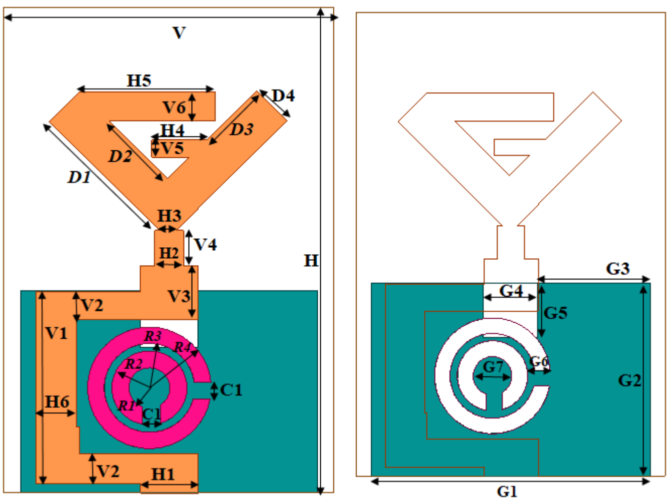

(a) (b)

Fig. 1. Geometry of the Single Patch Antenna
(a) Radiating Patch (b) Ground

TABLE I
ANTENNA GEOMETRICAL SPECIFICATIONS

Parameter	V	H	V1	V2	V3
Value (mm)	4	6	2.5	0.35	0.65
Parameter	V4	V5	V6	H1	H2
Value (mm)	0.45	0.2	0.4	0.7	0.35
Parameter	H3	H4	H5	H6	D1
Value (mm)	0.2	0.65	1.65	0.5	2
Parameter	D2	D3	D4	C1	R1
Value (mm)	1	0.8	0.5	0.14	0.25
Parameter	R2	R3	R4	G1	G2
Value (mm)	0.45	0.55	0.75	3.6	2.5
Parameter	G3	G4	G5	G6	G7
Value (mm)	1.45	0.7	1	0.3	0.5

B. Antenna Modeling : Step by step approach

The antenna design evolution into three distinct steps are mentioned in Fig. 2. and its associated return loss parameter represented in Fig. 3.

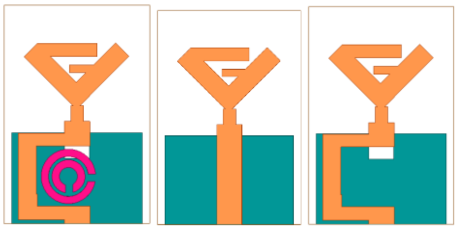
(a) (b) (c)

Fig. 2. (a) Stage1 (b) Stage2 (c) Stage3

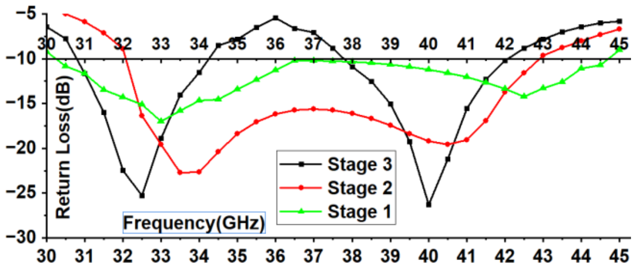

Fig. 3. S11 parameters for each stage

Stage 1: The initial stage configuration.

It comprises the modified Y-shaped radiator acts as an inductive–capacitive resonator, where the diagonal arms provide inductive loading and the horizontal branches with both arms introduces capacitive coupling with the adjacent arms. This interaction can be modeled as LC resonant circuit, it shows a resonance at the mentioned operating band in Fig 3. The narrow stem connecting the radiator to the feed further contributes to impedance transformation, enhancing bandwidth while maintaining proper matching. Thus, the proposed radiator achieves wideband operation with LC resonance effects.

Stage2: Analyze with meandered feed line structure

Ant-1 fails to exhibit strong resonance within the desired operating bandwidth. The meandered structure in the feed line increased its electrical length without enlarging the antenna's footprint, resulting good impedance matching in Ant-2, illustrated in Fig. 2(b). Ant-2 successfully achieves an operating bandwidth spanning 30 to 43 GHz.

Stage3: Notch band with Split ring resonator

Split-ring resonators (SRRs) are commonly used in printed antennas to realize functions such as circular polarization, bandwidth enhancement, and suppression of unwanted frequency bands by exploiting their resonant behavior. An SRR is a subwavelength resonant structure that can be modeled using an equivalent RLC circuit, where the metallic ring provides inductance and the split gap introduces capacitance.

As reported in the literature [29]–[31], the resonant behavior of SRRs depends strongly on their placement. When positioned near the feed line, an SRR couples efficiently to the incident magnetic field and exhibits low impedance at resonance, acting as a shunt resonator. This interaction leads to impedance mismatch and produces a well-defined notched band in the return-loss response, allowing selective rejection of unwanted signals while preserving the antenna's wideband performance.

This RLC branch accurately models the SRR-induced energy confinement and stopband behavior, consistent with established SRR coupling theory and metamaterial antenna models [32]–[35]. Hence, the circuit effectively explains the measured and simulated notch characteristics in the proposed antenna.

To generate a notch band in the range of 35–38 GHz with a center frequency of 36 GHz, the dimensions of the SRR were optimized so that it resonates precisely at the desired frequency of 36 GHz.

The proposed antenna employs an effective patch width Wp=1.65, length Lp=2 mm, and a substrate height of h=1.6 mm using RT/Duroid 5880. The effective dielectric constant is evaluated from Eq. (1).

$$\varepsilon_{eff} = \frac{\varepsilon_r+1}{2} + \frac{\varepsilon_r-1}{2}\frac{1}{\sqrt{1+12(\frac{h}{w})}} \approx 1.7688 \quad (1)$$

Using Eq. (2), the fringing field extension is predicted.

$$\Delta L = 0.412h\frac{(\varepsilon_{eff}+0.3)(\frac{Wp}{h}+0.264)}{(\varepsilon_{eff}-0.258)(\frac{Wp}{h}+0.8)} \approx 0.6386 \text{ mm} \quad (2)$$

Hence, the effective resonant length becomes $L_{eff} = L_p + 2\Delta L$ = 3.27 mm, The resonant frequency, determined by L_{eff} and ε_{eff}, is evaluated using Eq. (3)

$$f_r = \frac{c}{L_{eff}\sqrt{\varepsilon_{eff}}} \approx 34.4\text{GHz} \quad (3)$$

For $\frac{Wp}{h} > 1$, the characteristic impedance is estimated with Eq.(4).

$$Z_0 = \frac{120\pi}{\sqrt{\varepsilon_{eff}(\frac{Wp}{h}+1.393+0.667\ln(\frac{Wp}{h}+1.444))}} \approx 93.6\mathbf{\Omega} \quad (4)$$

The lumped equivalent parameters corresponding to the radiating patch are obtained using Eqs. (5) and (6).

$$L_{rad} = \frac{Z_0}{\omega_0} \approx 0.433nH \quad (5)$$

$$C_{rad} = \frac{1}{Z_0\omega_0} \approx 0.0494pF \quad (6)$$

The approximate radiation resistance can be calculated with Eq.(7).

$$R_{rad} = \frac{90}{\varepsilon_{eff}^2}\left(\frac{L_p}{w_p}\right)^2 \approx 42.3\Omega \quad (7)$$

indicating efficient radiation performance, as it closely matches the 50 Ω feed line.

To ensure proper impedance transformation between the feed resistance (Rs = 50 Ω) and the antenna input resistance (Rrad ≈ 42.3 Ω), the matching network components (Lmatch and Cmatch) are obtained using Eqs(8),(9)

$$L_{match} = \frac{X_{series}}{\omega_0} \approx 0.10nH \quad (8)$$

and $C_{match} = \frac{B_{Shunt}}{\omega_0} \approx 47fF$ (9)

here

$$Q_m = \sqrt{\frac{R_s}{R_L} - 1}$$

$$X_{series} = R_s\, Q_m$$

$$B_{shunt} = \frac{Q_m}{R_L}$$

which minimize reflection and maximize power transfer at resonance.

The SRR resonance is expressed using Eq. (10).

$$F_{SRR} = \frac{1}{2\pi\sqrt{L_{SRR}C_{SRR}}} \quad (10)$$

Where L_{SRR} is the effective ring inductance and C_{SRR} is the gap capacitance, determined by the split width and inter-ring spacing.

Following [35], the inductance of a conducting ring characterized by mean radius "a" and width "w" is approximated by Eq. (11).

$$L(w) = \mu_0[\ \ln\left(\frac{8a}{w}\right) - 2\ ] \quad (11)$$

For the present design with mean radius a=0.55 mm and conductor width w=0.2 mm , the inductance is computed as L≈0.754 nH .

The required capacitance to achieve resonance is calculated using Eq. (12). fr=36 GHz is

$$C_{req} = \frac{1}{(2\pi f_r)^2 L} = 26.1\text{fF} \quad (12)$$

As reported in [32], the split-gap capacitance corresponding to a gap width "d" is approximated through Eq. (13).

$$C_{gap}(d,w) = \frac{4\varepsilon_0\varepsilon_{eff}}{\pi}\ln\left(\frac{4w}{d}\right)h \quad (13)$$

where h=1.6 mm is the substrate thickness and εeff is the effective dielectric constant was 1.62

For εr=2.2(RT/Duroid 5880 substrate), h=1.6 mm, and w=0.20mm, the required capacitance of 26.1 fF is obtained when the split width is d(G1) ≈ 0.131 mm .

Equation (14) is used to determine the resistance of the split-ring resonator.

$$R_{SRR} = QX_L(\omega_0) = 2033\ \Omega \quad (14)$$

That resistance represent the equivalent damping or loss of the SRR resonance , where the high resistance value (≈ 2033 Ω) represents the weak damping of the resonant current rather than a direct conduction path. At resonance, the SRR stores electromagnetic energy and behaves as a high-impedance trap, thereby suppressing signal transmission at that frequency.

C. Equivalent Circuit Modeling

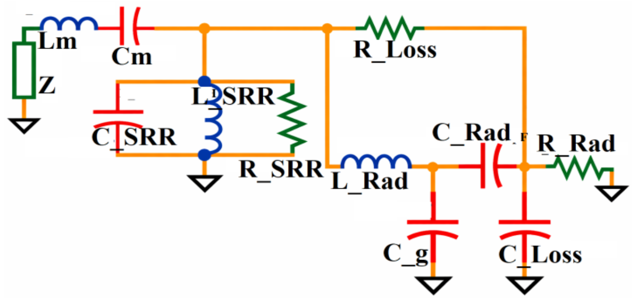

Fig. 4. RLC equivalent circuit for the proposed design

The equivalent circuit of the proposed antenna, which comprises a meandered feed line, a modified Y-shaped radiating patch, and an associated split-ring resonator (SRR), is shown in the Fig.4 The final dimensions and corresponding equivalent circuit parameters were derived using the transmission line model and related analytical concepts based on the proposed design and represented in table II.

TABLE II
EQUIVALENT LUMPED ELEMENTS OF THE PROPOSED ANTENNA

Parameter	ε_{eff}	ΔL	Z_0	L_{match}
Value(approx)	1.76	0.6mm	93.6 Ω	0.1nH
Parameter	L_{rad}	C_{rad}	R_{rad}	L_{eff}
Value(approx)	0.43nH	0.04pF	42.3 Ω	3.2mm
Parameter	L_{SRR}	C_{SRR}	R_{SRR}	C_{match}
Value(approx)	0.75nH	26.1fF	2k Ω	46fF
Parameter	Mean radius(a)	Ring width(w)	Spit gap (d)	
Value(approx)	0.55mm	0.2mm	0.13mm	

D. Verification of Stopband Formation

Full-wave simulations confirmed that the SRR resonates near 36 GHz, as shown in Fig. 3. The surface current distribution in Fig.5(a),5(b) indicates strong energy confinement around the SRR, causing a suppression band from 34.3 GHz to 37.7 GHz, while the patch maintains a wideband response outside this range.

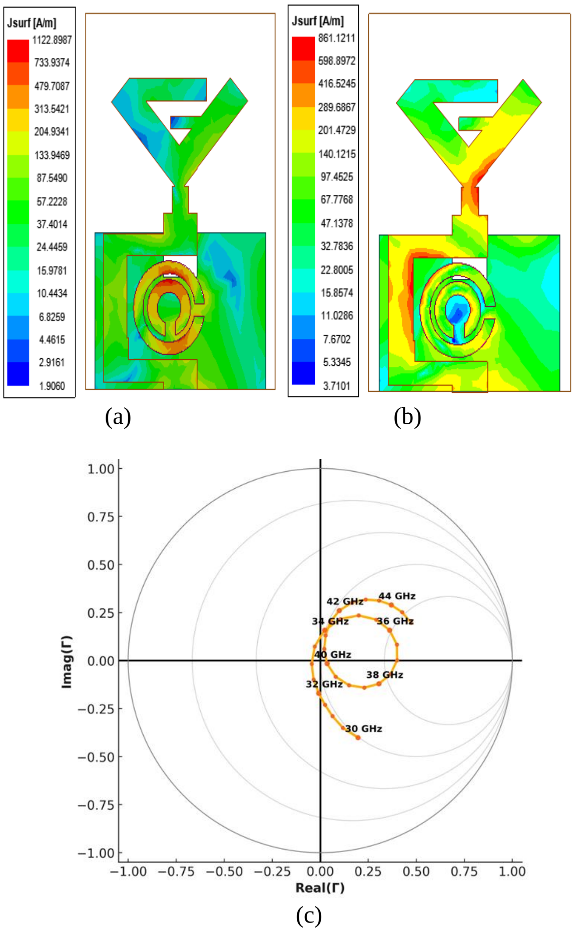

Fig. 5 . Surface current distribution at (a) 36GHz, (b) 33GHz, (c) ADS impedance verification (smith-chart)

The Smith chart obtained from the ADS equivalent circuit Fig.5(c), based on transmission line model parameters, shows a similar impedance trend to the HFSS results with minor deviations at lower frequencies due to modeling simplifications. The impedance locus shifts outward near 36 GHz, confirming strong reflection at the stopband, and remains close to the center elsewhere, validating the SRR-induced stopband and the reliability of the equivalent model.

III. MULTI INPUT MULTI OUTPUT ANTENNA

The ability of multiple-output (MIMO) antenna systems to improve data speeds, spectrum efficiency, and link dependability has made them indispensable in contemporary wireless communication.

A. Four Port MIMO Antenna

The geometry of the proposed four-port MIMO configuration is shown in Fig. 6. Figs. 6(a) and 6(b) illustrate the top and bottom views of the MIMO design. The detailed dimensions of MIMO antenna listed in table.

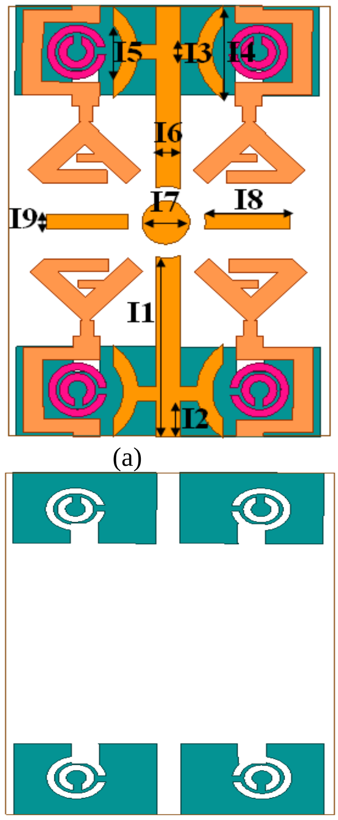

Parameter	**I1**	**I2**	**I3**	**I4**	**I5**
Value (mm)	5	1	0.4	2.6	1.5
Parameter	**I6**	**I7**	**I8**	**I9**	
Value (mm)	0.6	1.2	2.2	0.4	

Fig. 6. MIMO antenna geometry (a) Radiating Patch (b) Ground

B. Analysis of the isolation structure

Inter-element isolation is a key factor governing MIMO antenna performance. In the proposed design, conventional diagonal and orthogonal element arrangements reported in the literature were found to be ineffective, as the close proximity between one radiator and the split-ring resonator of an adjacent element disturbed impedance transformation and degraded isolation. To address this issue, the element layout and decoupling strategy were systematically optimized.

Surface current analysis (Fig. 7) shows that at lower frequencies the current is mainly concentrated along the feed line and radiator neck, while at the notched band it is strongly confined within the split-ring resonators. At higher frequencies, the current spreads over the radiator surface. Based on these observations, multiple isolation measures were implemented: the feed lines were repositioned to opposite substrate edges, arc-shaped parasitic structures were placed near the SRRs to confine radiated energy, and the isolation structure was extended toward the substrate center to suppress inter-element coupling. In addition, a circular decoupling slot with auxiliary gaps was etched at the substrate center to interrupt residual coupling paths. As a result, the proposed MIMO antenna achieves consistently high isolation exceeding −22 dB across the operating band, as illustrated in the corresponding Fig.7(g).

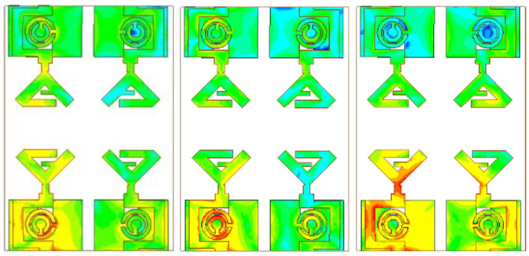

(a) (b) (c)

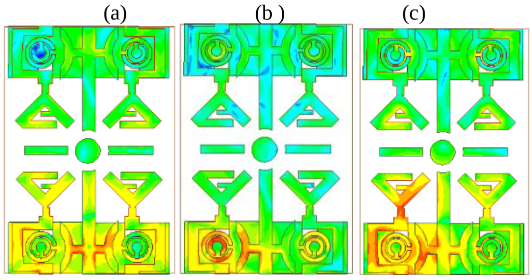

(d) (e) (f)

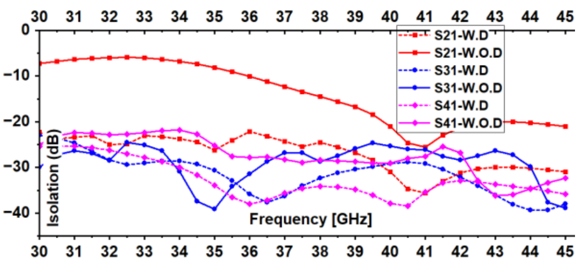

(g)

W.D : With Decoupling Structure W.O.D: With out Decoupling Structure

Fig. 7. Current Distribution:
without Decoupling Structure at (a) 33GHz, (b) 36.5GHz, (c) 41GHz; with Decoupling Structure at (d) 33GHz, (e) 36.5GHz, (f) 41GHz, (g) Isolation Levels Comparison

IV.RESULTS AND DISCUSSION

A fabricated Prototype of the proposed antenna was show in figure 8(a) ,8(b). Because of the physical size constraints, the S-parameters had to be recorded in different stages. The associated antenna configurations for each stage are presented in Figures 9(a), 9(b), and 9(c).

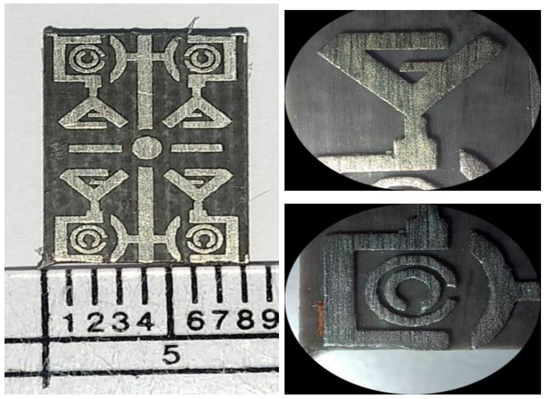

(a)

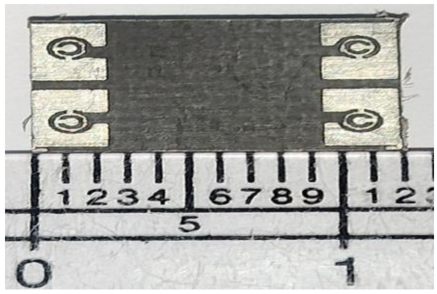

(b)

Fig. 8. Fabricated four port antenna (a) Radiating Patch, (b) Ground

(a) (b) (c)

Fig. 9. Fabricated antenna to measure (a) S11 and S12 parameters, (b) S13 Parameters, (c) S14 parameters.

These antennas were tested using a vector network analyzer (Keysight N5224B PNA) and in an anechoic chamber, as shown in Figs. 10(a)–10(b).

(a)

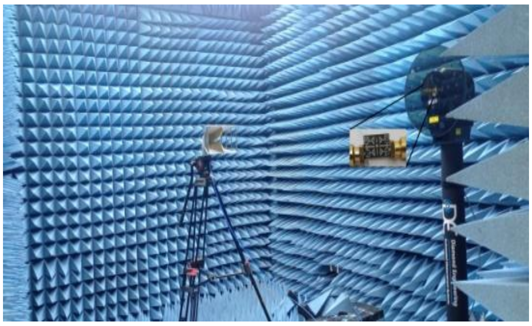

(b)

Fig. 10. (a) S-parameters Measurement using Vector Network Analyzer, (b) Radiation Characteristics Measurement using Anechoic Chamber

A. S-Parameter Verification

The comparison between simulated and measured S-parameters (S11, S12, S13, and S14) shown in Fig. 11(a) demonstrates excellent agreement. The measured reflection coefficient (S11) stays below –10 dB across the 30–42.5 GHz range, with a distinct notch band observed between 35 and 38.5 GHz, confirming a wide impedance bandwidth along with the desired band rejection.

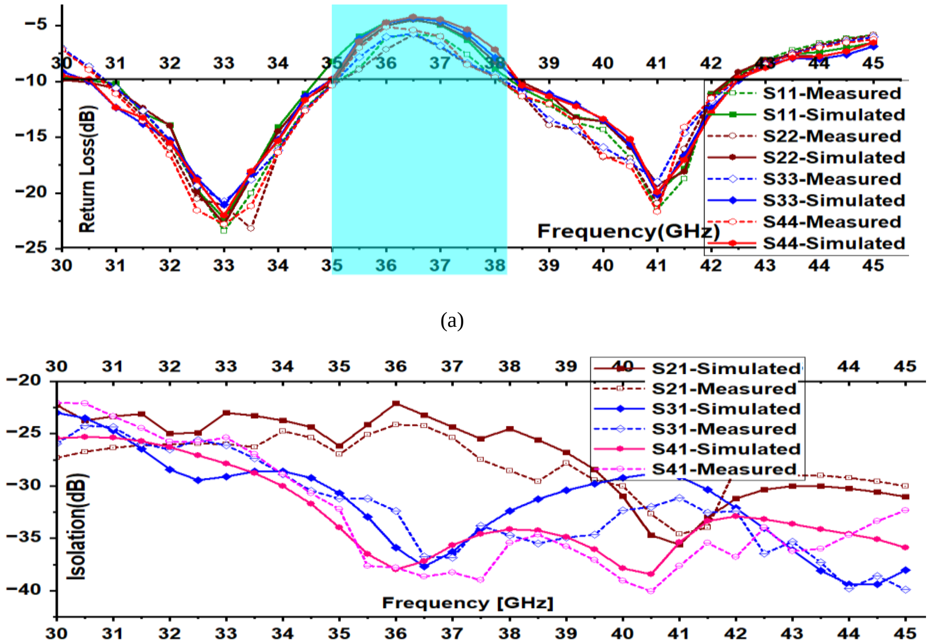

(a) (b)

Fig. 11. Comparison of simulated and measured S-parameter (a) Return Loss, (b) Isolation

This behavior closely matches the simulated results. As illustrated in Fig. 11(b), the isolation between antenna elements exceeds 22 dB across the entire operating band, validating the effective suppression of mutual coupling. The minor deviations between simulated and measured responses are mainly attributed to connector losses, fabrication tolerances, and measurement setup constraints.

B. Gain and radiation efficiency

The MIMO antenna gain characteristics are depicted in Figure 12(a), showing variations between 5 dB and 6.2 dBi, peak gain of 6.2dBi achieved at 42GHz. Antenna efficiency, a key metric for assessing performance, is presented in Figure 12(b), with values ranging from 85% to 88% across the operating frequencies

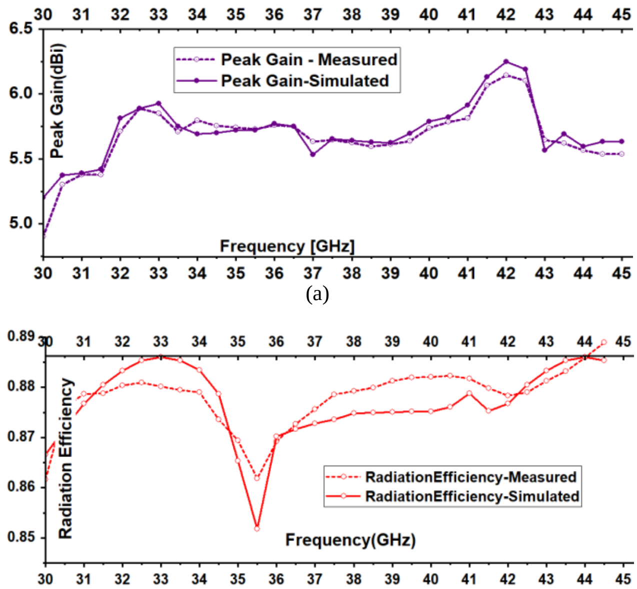

(a) (b)

Fig. 12. (a) Peak Gain (b) Radiation efficiency

C. Radiation Pattern

Fig.13 presents the radiation pattern of the proposed antenna, illustrating the spatial distribution of radiated power and providing clear insight into its directional characteristics.

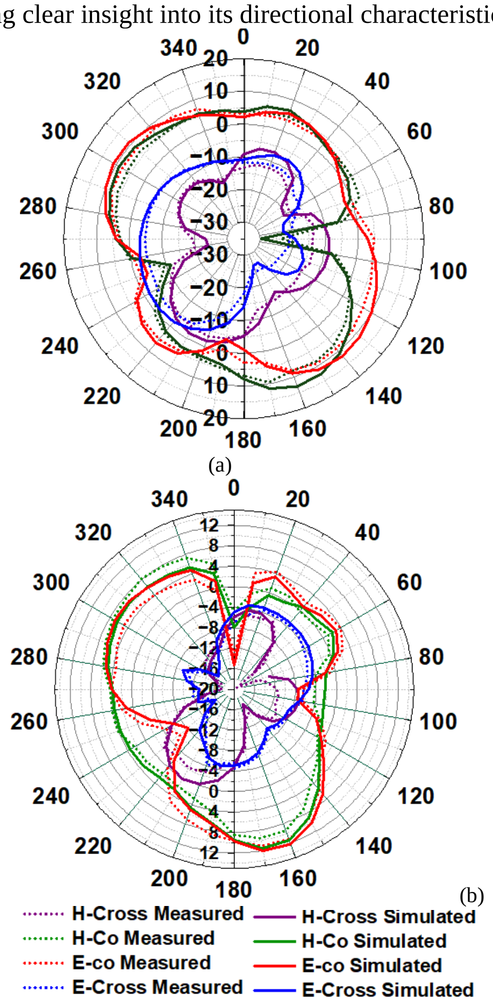

Fig. 13. 2D pattern at (a) 33 GHz (b)at 41 GHz

At the resonant frequencies, the measured radiation patterns show that the co-polarized field components dominate substantially over the cross-polarized components. This pronounced disparity indicates high polarization purity and minimal depolarization effects. Such behavior confirms that the antenna maintains stable and well-defined radiation characteristics across its operating bands, thereby demonstrating its excellent electromagnetic performance and suitability for practical wideband applications.

D. Diversity Performance

The diversity performance of the proposed antenna system was evaluated through key metrics, including the envelope correlation coefficient (ECC), diversity gain (DG). *Envelope correlation coefficient (ECC) and Diversity gain (DG).*

The ECC, which indicates the similarity between radiation patterns of antenna elements, should ideally be below 0.5 for effective diversity operation. In this design, both simulated and measured ECC values remain below 0.02 across the entire band, as illustrated in Fig. 14(a), confirming excellent isolation and low correlation between elements. The DG, which reflects the reliability of communication links through independent fading paths, ideally approaches 10 dB. As shown in Fig. 14(b), the proposed antenna consistently achieves DG values exceeding 9.975 dB, demonstrating strong diversity performance and reliable MIMO operation.

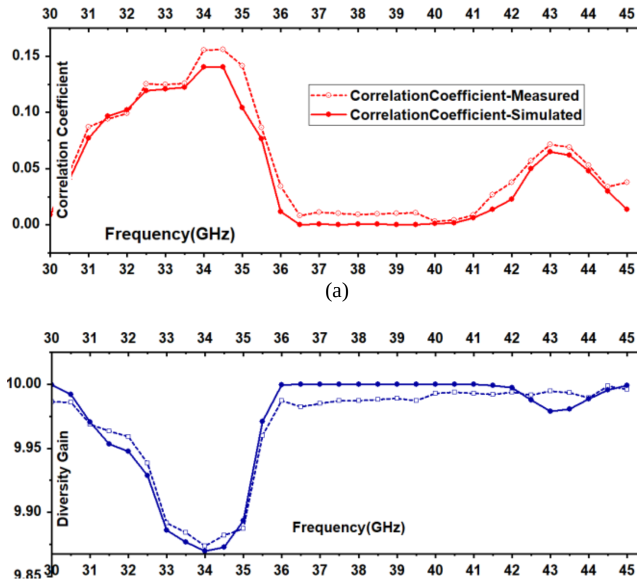

Fig. 14. Simulated Results (a) Effective Correlation Coefficient, (b) Diversity Gain

Performance comparison:

Table III compares the antenna in terms of overall size, bandwidth, isolation, ECC, and DG with previous designs.

TABLE III

COMPARISON OF THE ANTENNA IN TERMS OF OVERALL SIZE, BANDWIDTH, ISOLATION, ECC, AND DG WITH PREVIOUS designs

Refs.	Size (mm^3)	Bandwidth (GHz)	N.P	Effi(%)	Gain (dBi)	ECC	DG	Iso (dB)	Year
7	60 x 60 x 19.6	1.18–2.89	4	55-95	2.2-8.8	<0.01	------	<-20	2023
8	32.9x29.2x 0.254	20-40	2	-------	9.5-13.1	<0.0002	>9.98	<-20	2022
9	25x25x0.8	27.2-28.7 36.2-42	4	-------	6.5-10.2	<0.002		<-20	2025
10	27.6x12x0.274	26–30 36–41.5	2	--------	5-6.1	<0.03	>9.9	<-22	2022
11	43.6x43.6x0.4	27-29 37-40	4	96-99	3-6.1	<0.0002	>9.9	<-21	2022
13	31x31x5.4	12.8–45	4		0.5-9.8	<0.005	>9.9	<-23	2024
14	26x14x0.762	27.1-28.8 35.2-38.9	2		4.2-6.5	<0.00002	>9.9	<-34.6	2023
15	9.8x38.6x0.508	37-38.5	4	75-90	4.1-7.3	$<3x10^{-5}$	>9.9	<-30	2024

17	58.2x58.2x0.76	26.5-29	3	------	4.71-5.9	<0.01	-----	<-30	2022
18	23.85x23.85x0.254	19.6–22 29.2–30.3	4	>97	4.7-5.75	<0.19	>9.6	<-19	2022
19	34x22.5x0.508	24-31	2	75-91	4-6.8	<0.01	>9.5	<-25	2023
20	18x45.6x0.254	22-40	8	75-88	7-10.2	<0.0005	>9.99	<-18	2023
21	17x20x0.508	26-30 34-40	4	60-91	5.5-6.7	-------	---------	<-19	2022
22	15.3(radius) x1.16	26.1-27.5	3	------	4.9-5.2	<0.011	-----	<-19.3	2022
P.W	12x8x1.6	30-35 38.5-42.5	4	85-88	5.1-6.2	<0.02	>9.97	<-22	---------

*Refs –References , N.P – Number of Ports , Effi - Efficiency , Iso-Isolation , P.W – Proposed Work

CONCLUSION

An ultra-compact four-port ultra-wideband MIMO antenna is presented for millimeter-wave applications. The design employs a meandered feedline and an adjacent split-ring resonator to introduce a controlled notch band, while a dedicated decoupling structure improves inter-element isolation. The antenna operates over a wide bandwidth of 30–42.5 GHz with a rejection band from 35 to 38.5 GHz, within a compact size of $12 \times 8 \times 1.6$ mm³. Strong MIMO performance is achieved, with low mutual coupling, envelope correlation coefficient below 0.02. The antenna also provides a peak realized gain of 6.51 dBi. The operating band covers important mmWave frequencies, including 5G n260/n261, Ka-band satellite links, and short-range radar systems, while the notched band effectively suppresses interference from point-to-point and Ka-band services. This makes the proposed antenna suitable for compact mmWave communication platforms.

REFERENCES

[1] Alalewi, I. Dayoub, and S. Cherkaoui, “On 5g-v2x use cases and enabling technologies: A comprehensive survey,” IEEE Access, vol. 9,pp. 107 710–107 737, 2021.

[2] C. Zhu, G. Xu, A. Ren, W. Wang, Z. Huang and X. Wu, "A Compact Dual-Band Dual-Circularly Polarized SIW Cavity-Backed Antenna Array for Millimeter-Wave Applications," in *IEEE Antennas and Wireless Propagation Letters*, vol. 21, no. 8, pp. 1572-1576, Aug. 2022, doi: 10.1109/LAWP.2022.3174419

[3] N. K. Maurya, M. J. Ammann and P. Mcevoy, "Series-Fed Omnidirectional mm-Wave Dipole Array," in *IEEE Transactions on Antennas and Propagation*, vol. 71, no. 2, pp. 1330-1336, Feb. 2023, doi: 10.1109/TAP.2022.3232240.

[4] W. T. Sethi and S. H. Kiani, "Dual Band (28/38 GHz) Antenna Design for 5G mmWave Communication Networks," *2023 18th International Conference on Emerging Technologies (ICET)*, Peshawar, Pakistan, 2023, pp. 213-216, doi: 10.1109/ICET59753.2023.10374624.

[5] J. Li, Y. Zhu, Y. Shi, Y. Hu and W. Hong, "Millimeter-Wave Ultrawideband Antenna With Hybrid-Mode Resonance Including Microstrip Line, Slot, Patches, and Quasi-Monopole Modes," in *IEEE Antennas and Wireless Propagation Letters*, vol. 23, no. 5, pp. 1533-1537, May 2024, doi: 10.1109/LAWP.2024.3361902

[6] N. Alaa, R. A. Elsayed, K. F. A. Hussein and W. S. El-Deeb, "Dual-Band Millimeter-Wave Circularly Polarized Antenna for Mobile Communications," in *IEEE Access*, vol. 10, pp. 82119-82131, 2022, doi: 10.1109/ACCESS.2022.3196345.

[7] K. Arvind, K. B. Kumar, “High gain and enhanced isolation MIMO antenna with FSS and metasurface”, Optik, vol. 286, 2023. doi: 10.1016/j. ijleo. 2023. 170982

[8] Rania H. Elabd, Haythem H. Abdullah, “A High Mutual Coupling UWB MIMO Vivaldi Antenna Based on CSRR-NL for Contemporary 5G Millimeter-Wave Applications”, J Infrared Milli Terahz Waves, vol. 43, pp. 920–941, 2022. doi: 10.1007/ s10762- 022- 00894-y

[9] M. M. Basha, P. Pradeep, S. Gundala, and J. Syed “Design of compact and high gain dual-band four-port MIMO antenna array for mm-wave 5G Communications”, Results Eng, vol. 25, pp.104153 Mar. 2025. doi: 10.1016/j. rineng. 2025. 104153

[10] Ayman R. S. , Wael A. E. A. , and Ahmed A. I., “Minimally Coupled Two-Element MIMO Antenna with Dual Band (28/38 GHz) for 5G Wireless Communications”, Journal of Infrared, Millimeter,and Terahertz Waves vol. 43, pp. 335-348 2022. doi: 10. 1007/ s10762- 022-00857

[11] Aghoutane B., Sudipta D., Mohammed E. Gh., Madhav B. T. P., and Hanan E. F., “A Novel Dual Band High Gain 4-port Millimeter Wave MIMO Antenna Array for 28/37 GHz 5G Applications”, AEU-International Journal of Electronics and Communications , vol. 145, no. 4, p. 154071, 2022.

[12] U. Rafique, A. Shobit, N. Nasir, Kh. Hisham, and U. Khalil, “Inset-fed Planar Antenna Array for Dual-band 5G MIMO Applications”, Progress In Electromagnetics Research C, vol.112, ,pp. 83-98,2021.

[13] S. Angadi, Y. Sharma, N.S. Raghava, and T. Sabapathy, “low profile circularly polarized metasurface-based ultra-wideband 4x4 MIMO antenna for 5G NR band FR2 frequencies” AEU - Int J ElectronCommun, Vol. 178, pp., 15528, May 2024. doi: 10. 1016/j.aeue.2024. 155282

[14] B. A. F. Esmail and S. Koziel, “Design and optimization of metamaterialbased dual-band 28/38 GHz 5G MIMO antenna with modified ground for isolation and bandwidth improvement,” *IEEE Antennas Wireless Propag. Lett.*, vol. 22, pp. 1069–1073, 2023.

[15] A. K. Singh and S. Pal, “Compact self-isolated extremely low ECC folded-SIW-based slotMIMOantenna for 5G application,” *IEEE Antennas Wireless Propag. Lett.*, vol. 23, pp. 194–198, 2024.

[16] M. Usman, E. Kobal, J. Nasir, Y. Zhu, C. Yu, and A. Zhu, “Compact SIW fed dual-port single element annular slot MIMO antenna for 5G mmWave applications,” *IEEE Access*, vol. 9, pp. 91995–92002, 2021, doi: 10.1109/ACCESS.2021.3091835.

[17] E. Kobal, R.-J. Liu, C. Yu, and A. Zhu, “A high isolation, low-profile, triple-port SIW based annular slot antenna for millimeter-wave 5G MIMO applications,” *IEEE Access*, vol. 10, pp. 89458–89464, 2022.

[18] M. A. Sofi, K. Saurav, and S. K. Koul, “Four-port orthogonal circularly polarized dual-band MIMO antenna with polarization and spatial diversity using a dual-band linear-to-circular polarization converter,” *IEEE Trans. Antennas Propag.*, vol. 70, no. 9, pp. 8554–8559, Sep. 2022.

[19] R. N. Tiwari, V. Kaim, P. Singh, T. Khan, and B. K. Kanaujia, “Semiflexible diversified circularly polarized millimeter-wave MIMO antenna for wearable biotechnologies,” *IEEE Trans. Antennas Propag.*, vol. 71, no. 5, pp. 3968–3982, May 2023.

[20] A. Khan, Y. He, and Z. Chen, “An eight-port circularly polarized wideband MIMO antenna based on a metamaterial-inspired element for 5G mmWave applications,” *IEEE Antennas Wireless Propag. Lett.*, vol. 22, no. 7, pp. 1572–1576, Jul. 2023.

[21] S. Sadeghi-Marasht, M. S. Sharawi, and A. Zhu, “Dual-band circularly polarized antenna array for 5G millimeter-wave applications,” *IEEE Open J. Antennas Propag.*, vol. 3, pp. 314–323, Mar. 2022.

[22] S. Tang, C.-Y.Chiu, andR.Murch, “A millimeter-wave tri-modal patch antenna,” *IEEE AntennasWireless Propag. Lett.*, vol. 21, no. 2, pp. 406–410, Feb. 2022, doi: 10.1109/LAWP.2021.3133689.

[23] N. Jawad and L. Markley, "A Single-Layer Frequency Selective Surface With Dual Wideband Band-Stop Response," in *IEEE Antennas and Wireless Propagation Letters*, vol. 19, no. 6, pp. 916-920, June 2020, doi: 10.1109/LAWP.2020.2982132

[24] K. Huang and Y. Zhang, "Analysis and Design of Dual-Polarized Millimeter-Wave Filtering Magneto-Electric Dipole Antenna," in *IEEE Transactions on Antennas and Propagation*, vol. 71, no. 8, pp. 6947-6952, Aug. 2023, doi: 10.1109/TAP.2023.3270717.

[25] C. Deng, X. Cao, D. Li and W. Yu, "Compact Dual-Band MIMO Antenna With Shared Decoupling Structure for 5G Mobile Terminals," in *IEEE Antennas and Wireless Propagation Letters*, vol. 22, no. 6, pp.

1281-1285, June 2023, doi: 10.1109/LAWP.2023.3240673.

[26] M. Koohestani, N. Azadi-Tinat and A. K. Skrivervik, "Compact Slit-Loaded ACS-Fed Monopole Antenna for Bluetooth and UWB Systems With WLAN Band-Stop Capability," in *IEEE Access*, vol. 11, pp. 7540-7550, 2023, doi: 10.1109/ACCESS.2023.3238577.

[27] D. Li, C. Yang, Y. Liu, L. Yang and Q. Chen, "Planar Printed Wideband Filtering Quasi-Yagi Antenna and Its Notch-Band Design Using Parasitic Elements for Vehicular Communication," in *IEEE Transactions on Vehicular Technology*, vol. 73, no. 2, pp. 2122-2131, Feb. 2024, doi: 10.1109/TVT.2023.3314974.

[28] H. T. Chattha, F. Latif, F. A. Tahir, M. U. Khan and X. Yang, "Small-Sized UWB MIMO Antenna With Band Rejection Capability," in *IEEE Access*, vol. 7, pp. 121816-121824, 2019, doi: 10.1109/ACCESS.2019.2937322

[29] S. Gupta and R. K. Chaudhary, "EBG and SRR loaded triple band notched UWB antenna," Scientia Iranica, vol. 29, no. 5, pp. 2504–2513, Sept. 2022.

[30] H. F. A. El-Banna, S. I. A. El-Hamid, and M. E. Nasr, "SRR metamaterial-based broadband patch antenna for wireless communications," Journal of Engineering and Applied Science, vol. 69, no. 1, pp. 1–10, 2022.

[31] D. Patel, R. K. Chaudhary, and M. K. Jha, "Slot and SRR-Loaded Quad-Port, Hen-Shaped Fractal UWB-MIMO Antenna with Quad Band-Reject Ability," Iranian Journal of Science and Technology, Transactions of Electrical Engineering, vol. 47, pp. 499–510, Mar. 2023.

[32] J. B. Pendry, A. J. Holden, D. J. Robbins, and W. J. Stewart, "Magnetism from conductors and enhanced nonlinear phenomena," *IEEE Transactions on Microwave Theory and Techniques*, vol. 47, no. 11, pp. 2075–2084, Nov. 1999.

[33] T. C. Edwards and M. B. Steer, *Foundations of Interconnect and Microstrip Design*, 3rd ed. Hoboken, NJ, USA: Wiley, 2000.

[34] D. M. Pozar, *Microwave Engineering*, 4th ed. Hoboken, NJ, USA: Wiley, 2012.

[35] F. W. Grover, *Inductance Calculations: Working Formulas and Tables*. New York, NY, USA: Dover, 2004